


 Cite this: *Chem. Commun.*, 2025, 61, 8671

 Received 3rd March 2025,
 Accepted 9th May 2025

DOI: 10.1039/d5cc01147g

rsc.li/chemcomm

Light intensity–directed selective CO₂ photoreduction using iron(0)–zirconium dioxide photocatalyst†

 Tomoki Oyumi,  Ikki Abe,  Masahito Sasaki and Yasuo Izumi *

Selective photoreduction of CO₂ to CO, CH₄, and C₂₋₃ paraffins was directed by increasing ultraviolet-visible light intensity over an Fe–ZrO₂ photocatalyst. Fe⁰ nanoparticles sequentially reduced COH—transferred from the ZrO₂ surface—into CH_x species and hydrocarbons, facilitated by light-induced heating to ~452 K.

Photocatalytic CO₂ reduction establishes a novel C-neutral cycle and is considered a potential environmental solution for a sustainable society.^{1,2} However, its near-term implementation is hindered by economic challenges, primarily due to the costs of photocatalysts and reactor design.^{3,4} Among first-row transition metals, Fe is the most abundant and cost-effective. Consequently, Fe-based photocatalysts for CO₂ photoreduction have been widely studied. However, nearly all reported systems employ Fe in the form of metal ions within metal–organic frameworks, covalent organic frameworks, porphyrins, or as Fe₂O₃, functioning primarily as redox mediators (Table S1, ESI†).⁵

In this study, a Fe⁰ surface was evaluated as a CO₂ photoreduction catalyst for C₁₋₃ hydrocarbons (HCs) in combination with semiconductor ZrO₂. An Fe₃O₄–ZrO₂ composite was synthesized *via* a liquid-phase reduction method, using Fe(NO₃)₃·9H₂O as the precursor and reducing it at 973 K under H₂ to obtain the Fe⁰ (7.5 wt%)–ZrO₂-973R photocatalyst. The valence state and coordination of Fe were monitored during synthesis using X-ray absorption near-edge structure (XANES) and extended X-ray absorption fine structure (EXAFS).

This approach facilitated the formation of bifunctional sites—O vacancies (V_O[•]) on the ZrO₂ surface^{3,6-9} and Fe⁰ nanoparticles—enabling the selective photogeneration of CO and C₁₋₃ HCs from CO₂. At a ultraviolet-visible (UV-Vis) light intensity of 110 mW cm⁻², using ¹³CO₂ and H₂ gases with the Fe⁰ (7.5 wt%)–ZrO₂-973R photocatalyst, both ¹³CO and ¹³CH₄

were gradually generated over the first 5 h of photoreaction (Table 1a). However, beyond this period, ¹³CO formation became predominant (>99 mol% selectivity; entry a'), as subsequent reaction steps from CO did not proceed (Scheme 1a). The steady photogeneration of CO was significantly faster than that observed with ZrO₂ alone (Table S2a, ESI†),⁶⁻⁸ confirming the active role of the Fe⁰ surface, but the selectivity change after 5 h seemed due to strong CO₂ adsorption on it in CO₂ photoreduction (see below).

In stark contrast, increasing the irradiated light intensity to 322 mW cm⁻² shifted the Fe⁰–ZrO₂-973R photocatalyst from selective two-electron reduction to ¹³CO to predominant eight-electron reduction to ¹³CH₄ production (>95 mol% selectivity; Table 1b). This shift occurred because the hydrogenation steps from CO proceeded rapidly under higher light intensity, facilitating the sequential reduction from CO₂ to CO and ultimately to CH₄. From a practical perspective, however, the ¹³CH₄ light-induced synthesis using Fe⁰–ZrO₂ requires further improvement, as photocatalytic activity declined after 5 h of photoreaction—more so than under 110 mW cm⁻² irradiation (Table 1a' and b'). As no CH_x species were observed in the Fourier transform infrared (FTIR) spectrum under the conditions, this deactivation was attributed to Fe⁰ surface poisoning by strongly adsorbed CO₂ (Scheme 1b).

To enhance the stability of the Fe⁰–ZrO₂-973R photocatalyst, the irradiated light intensity was further increased to 472 mW cm⁻². Under these conditions, the ¹³CH₄ formation rate reached 170 μmol h⁻¹ g_{cat}⁻¹ with >71 mol% selectivity, accompanied by ¹³CO formation at 69 μmol h⁻¹ g_{cat}⁻¹ (>28 mol% selectivity) over 5 h of photoreaction (Fig. 1A and Table 1c). Over time, ¹³CH₄ formation exhibited a turning point at ~5 h of photoreaction (Fig. 1A), attributed to partial Fe⁰ site poisoning by intermediate species such as HCO₂ and CH_x. Beyond this period, the ¹³CH₄ formation rate stabilized at 20 μmol h⁻¹ g_{cat}⁻¹ with >49 mol% selectivity (Table 1c' and Scheme 1c). Under the steady conditions, CO₂ blocking on Fe⁰ sites should be less effective in contrast to the status under 110–322 mW cm⁻² irradiation. This time-dependent product distribution confirmed a consecutive

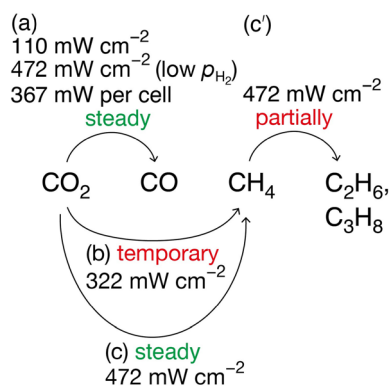
Department of Chemistry, Graduate School of Science, Chiba University, Yayoi 1-33, Inage-ku, Chiba 263-8522, Japan. E-mail: yizumi@faculty.chiba-u.jp

† Electronic supplementary information (ESI) available: Lists of reported photo- and thermal catalysts, experimental details, photocatalytic time course, X-ray diffraction, and optical, X-ray absorption, and FTIR spectroscopy of photocatalyst and surface species. See DOI: <https://doi.org/10.1039/d5cc01147g>



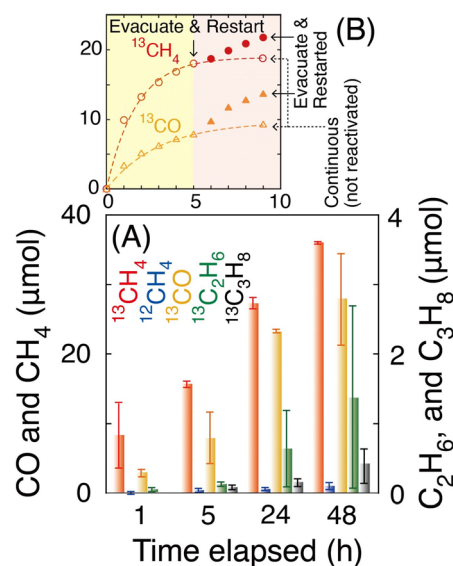
Table 1 CO₂ photoreduction outcomes using Fe (7.5 wt%)-ZrO₂ prereduced at 973 K in the presence of either H₂ or H₂O

Entry	Reactant	Reductant	Light intensity (mW)	Stage of reaction test (h)	Formation rate ($\mu\text{mol h}^{-1} \text{g}_{\text{cat}}^{-1}$)				
					¹³ CO	¹³ CH ₄	¹³ C ₂ H ₆	¹³ C ₃ H ₈	O ₂
a	¹³ CO ₂ (2.3 kPa)	H ₂ (21.7 kPa)	110 cm ⁻²	0–5	3.7	3.8	0.052	0.018	< 0.002
a'				5–48	3.7	< 0.002	< 0.002	< 0.002	
b			322 cm ⁻²	0–5	2.4	45	0.20		
b'				5–48	1.7	1.1	0.036		
c			472 cm ⁻²	0–5	69	170	2.1	0.30	
c'				5–48	18	20	2.3	0.56	
c''				(20–48)	(2.7)	(16)	(2.6)	(0.70)	
d			1510 cm ⁻²	0–5	35	40	0.26	< 0.002	< 0.002
d'			(with water bath)	5–48	5.2	0.41	0.037		
e	CO ₂ (95 kPa)	H ₂ O (70 mL)	367 per cell	0–5	CO	CH ₄	C ₂ H ₆	C ₃ H ₈	O ₂
e'				5–48	12	< 0.002	< 0.002		64
					8.5	0.86			9.0

**Scheme 1** Temporary and steady CO₂ photoreduction pathways directed by irradiated light intensity (110–472 mW cm⁻²) using the Fe⁰ (7.5 wt%)-ZrO₂-973R photocatalyst in presence of H₂ ((a)–(c) and (c')) or H₂O (a).

reaction pathway: CO₂ reduction to CO, followed by CH₄ formation, and subsequent conversion to C_{2,3} hydrocarbons. Between 20 and 48 h of photoreaction, the ¹³CH₄ formation rate remained stable (> 73 mol% selectivity), while ¹³C₂H₆ and ¹³C₃H₈ selectivity significantly increased to 15 mol% (total formation rate: 3.3 $\mu\text{mol h}^{-1} \text{g}_{\text{cat}}^{-1}$), effectively suppressing initial ¹³CO production (Table 1c'' and Scheme 1c'). Notably, no C₂H₄ or C₃H₆ was detected. Furthermore, photocatalytic activity could be restored by a 1-h evacuation at 10⁻⁶ Pa under light, reactivating the consecutive reduction process from CO to CH₄ (Fig. 1B).

The other photocatalytic test was using CO₂ (2.3 kPa), H₂ (21.7 kPa), and the light irradiation at 1510 mW cm⁻², but the quartz reactor was cooled with water bath (Table 1d–d' and Chart S1, ESI[†]). The ¹³CO and ¹³CH₄ formation rates were 24–51% of corresponding rates without water cooling until 5 h of reaction (Table 1c and c'), while the decline after 5 h was more significant, especially for ¹³CH₄ formation, strongly suggesting that charge separation in/on ZrO₂ owing to light proceeded CO₂ reduction while Fe nanoparticle surface at lower temperature in thermal equilibrium with ZrO₂, reactor, and 2.5 L of water was deactivated for subsequent multiple hydrogenation earlier by adsorbed species, e.g. CO₂. The increase of water temperature was minimal: from 295.2 to 295.5 K during the photocatalytic test for 48 h (Chart S1, ESI[†]).

**Fig. 1** (A) and (B) Time course of ¹³CO, ¹³CH₄, ¹²CH₄, ¹³C₂H₆, and ¹³C₃H₈ formation using Fe⁰ (7.5 wt%)-ZrO₂-973R, ¹³CO₂ (2.3 kPa), H₂ (21.7 kPa), and UV-Vis light irradiation at 472 mW cm⁻². (B) Comparison with the reactivation test (filled symbols) after 1 h of catalyst evacuation under UV-Vis light irradiation at the 5-h mark.

Steady photocatalytic CO₂ reduction was also achieved using H₂O as the reductant instead of H₂ under UV-Vis light irradiation at 367 mW per cell. CO was continuously generated at a rate of 12–8.5 $\mu\text{mol h}^{-1} \text{g}_{\text{cat}}^{-1}$ (Table 1e and e'), proceeding more rapidly than the multiple hydrogenation steps required for CH₄ formation over Fe⁰ (selectivity < 9.2 mol%; Scheme 1a and Fig. S1, ESI[†]). This was attributed to the predominant presence of H₂O rather than H at the Fe⁰ surface, which favored CO generation over further hydrogenation to CH₄.

The effects of UV-Vis light irradiation on the Fe⁰-ZrO₂-973R photocatalyst were investigated. In the UV-Vis absorption spectra of the Fe₃O₄-ZrO₂ sample (Fig. S2b, ESI[†]), two absorption shoulders at 410 and 525 nm, attributed to Fe²⁺ and Fe³⁺ ions, were observed, whereas ZrO₂ alone exhibited no visible light absorption (spectrum a). This spectral profile was consistent with the reported absorption spectrum of Fe₃O₄.¹⁰ Upon H₂ treatment at 973 K, absorption extended across the entire visible region



(spectrum c), and the spectrum remained similar after 48 h of photocatalytic $^{13}\text{CO}_2$ reduction (spectrum d), confirming the formation and stability of Fe^0 nanoparticles, which facilitated multiple hydrogenation steps from CO/COH species (Scheme 1c and c'). The Fe valence state assignments were corroborated by changes in the XANES spectrum, aligning with those of standard Fe^0 and Fe_3O_4 (Fig. S3A(c) and (d), ESI†).¹¹ EXAFS Fourier transform analysis of Fe^0 - ZrO_2 -973R revealed interatomic pairs characteristic of Fe^0 (Fig. S4, ESI†), while X-ray diffraction showed an Fe (011) peak overlapping with peaks corresponding to monoclinic ZrO_2 (Fig. S5, ESI†), further supporting the formation of Fe^0 active sites in the Fe^0 - ZrO_2 -973R photocatalyst.

The fluorescence emission spectra of Fe^0 - ZrO_2 -973R were measured under excitation at 200 nm (Fig. S6, ESI†), a wavelength corresponding to an energy higher than the band gap of ZrO_2 (Fig. S2a, ESI†). The spectrum exhibited both an interband excitation–deexcitation peak centered at 367 nm (spectrum a) and intraband transition peaks associated with impurity levels, such as O vacancies and Hf (0.55 wt%) in/on ZrO_2 , appearing at 451, 468, 481, 491, 528, and 623 nm. These emissions were significantly suppressed upon the addition of Fe_3O_4 and further reduced with Fe^0 nanoparticles (spectra b and c), indicating effective trapping of excited electrons at the conduction band (CB) of ZrO_2 .

Next, the reaction pathway from CO_2 to CO and HCs is considered. The role of $\text{V}_\text{O}^\bullet$ sites on the ZrO_2 surface in CO_2 adsorption and its subsequent photoreduction to OCOH and COH species was analyzed using density functional theory (DFT) calculations.⁹ The population of surface $\text{V}_\text{O}^\bullet$ sites was evaluated to one per 44 nm^2 based on $^{13}\text{CO}_2$ exchange amount with preadsorbed $^{12}\text{CO}_2$ on $\text{V}_\text{O}^\bullet$ site (0.070 μmol ; Table S3g and Fig. S7, ESI†). The population of surface $\text{V}_\text{O}^\bullet$ sites seems not vary much before and after photocatalytic test based on essentially negligibly-changing UV-visible and XRD data (Fig. S2c, d and S5a, b, ESI†). Consequently, this study focuses on the critical steps enabling transient or sustained C_{1-3} photogeneration (Scheme 1b and c), specifically the conversion of COH and/or CO into C_{1-3} HCs over the Fe^0 surface.

To identify the active sites responsible for these reaction steps, Fe K-edge EXAFS measurements were conducted on the Fe^0 - ZrO_2 -973R photocatalyst under CO_2 and H_2 exposure. Unexpectedly, $\sim 20\%$ of the Fe^0 sites reduced at 973 K were oxidized upon reaction with CO_2 in the dark, as indicated by EXAFS analysis (Fig. 2A, 0 min). The spectral fit, obtained by convolving standard XANES spectra for Fe^0 and FeO with an 8:2 mixing ratio (Fig. S3B(d), ESI†), aligned with the EXAFS data. This oxidation is attributed to the formation of an M-shaped Fe^{2+} -O-C(=Fe⁰)-O- Fe^{2+} species upon CO_2 adsorption on Fe. DFT calculations further support the energetic stability of this species on the Fe^0 (111) surface, with an adsorption energy of 0.92 eV and a Bader charge of +0.352 on Fe bonded to O, consistent with prior studies.¹² At this stage, CO did not desorb spontaneously from Fe surface and was not detected.

Upon UV-Vis light irradiation, the Fourier transform of EXAFS spectra (Fig. 2A, 0 min) showed that the Fe–O and Fe \cdots Fe peaks corresponding to FeO were rapidly replaced by

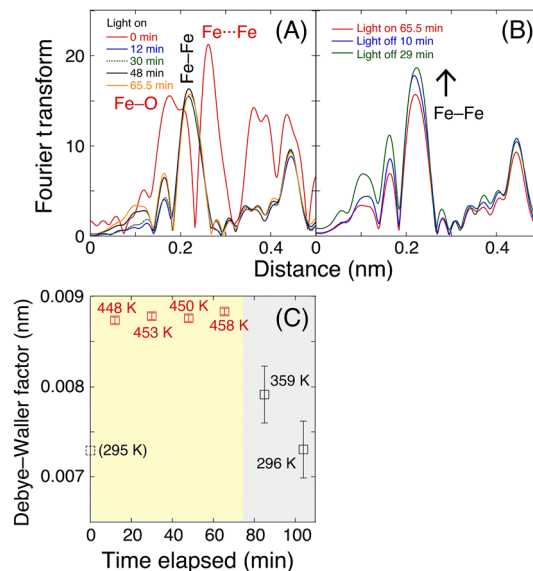


Fig. 2 Time-dependent Fourier transform of Fe K-edge EXAFS for Fe^0 (7.5 wt%)– ZrO_2 -973R under CO_2 (2.3 kPa), H_2 (21.7 kPa), and UV-Vis light irradiation (322 mW cm^{-2}). (A) During 75 min of illumination, (B) after the light was turned off, and (C) corresponding time-dependent evolution of the Debye–Waller factor for the Fe–Fe interatomic pair.

a metallic Fe–Fe peak at 0.21 nm (phase shift uncorrected; Fig. 2A, 12 min). This transformation indicates the reduction of Fe^{2+} in the M-shaped Fe^{2+} -O-C(=Fe⁰)-O- Fe^{2+} species.

In the FTIR spectrum of Fe^0 - ZrO_2 -973R under $^{13}\text{CO}_2$ and H_2 (Fig. S8, ESI†), shoulder peaks at 1584, 1396, and 1217 cm^{-1} corresponded to $\nu_{\text{as}}(\text{OCO})$, $\nu_{\text{s}}(\text{OCO})$, and $\delta(\text{OH})$ bending vibrations, respectively, were attributed to monodentate and bridging bicarbonate species adsorbed on the surface.^{6–8} In contrast, the broader peaks centered at 1538 and 1261 cm^{-1} were tentatively assigned $\nu_{\text{as}}(\text{OCO})$ and $\nu_{\text{s}}(\text{OCO})$ stretching vibrations of bidentate carbonate species on ZrO_2 ,¹³ as well as the M-shaped Fe–O-C(=Fe⁰)-O-Fe species proposed earlier, adsorbed at various sites on the Fe^0 surface. This assignment aligns with DFT-calculated O–C–O bond angles of 122° . Upon UV-Vis light irradiation (265 mW cm^{-2}), the peak associated with $^{13}\text{CO}_2$ and H_2 adsorption negatively shifted by 41 cm^{-1} . This shift was attributed to the reduction of Fe^{2+} to Fe^0 via electron transfer from ZrO_2 CB to Fe, followed by electron injection into the σ^* orbitals of C–O bonds, facilitating bond weakening and activation under UV-Vis illumination, in consistent with the reduction from Fe^{2+} to Fe^0 upon the light irradiation based on EXAFS (Fig. 2A).

The broad peak centered at 1497 cm^{-1} disappeared within 4 min under vacuum and UV-Vis light irradiation, likely due to CO_2 desorption, suggesting that CO_2 and carbonate species are not direct intermediates in C_{1-3} HC formation. In contrast, the conversion of adsorbed CO_2 on the ZrO_2 surface to COH species appears to be the rate-limiting step, as only methane (ν_3 peak at 3010 cm^{-1}) was detected alongside adsorbed CO_2 and bicarbonate species.

To elucidate the energetic origins of the multiple hydrogenation steps in which COH and/or CO species migrate over the Fe^0 surface to form HCs, the Fe–Fe coordination number was



determined *via* EXAFS as 5.3, corresponding to a surface dispersion of 0.95.¹⁴ In the correlated Debye model, the Debye temperatures of bulk and surface Fe (vertical motion) are reported as 467 K¹⁵ and 225 K,¹⁶ respectively. Using multiple scattering calculation code FEFF¹⁷ and plane-wave EXAFS analysis code XDAP,¹⁸ the local Fe site temperature during CO₂ photoreduction was experimentally monitored. Upon UV-Vis light irradiation, the Fe site temperature rapidly increased to ~452 (±35) K as hot spot due to light absorption and remained nearly constant at thermal equilibrium with the supporting ZrO₂ and the EXAFS cell both at ~295 K (Fig. 2C, left).

When the light was turned off, the heat generated by light energy dissipated, and the Fe site temperature returned to 296 K (Fig. 2C, right). This observation confirms that the selective formation of C₁₋₃ HCs in this study resulted from a two-step process: (i) CO₂ reduction to COH/CO *via* charge separation in ZrO₂^{3,6-8} and (ii) subsequent multiple hydrogenation of CO/COH on the Fe⁰ surface, which was maintained at ~452 K due to light absorption.

Thermal CO₂ hydrogenation and Fischer-Tropsch synthesis of HC(s) using Fe-based catalysts typically require reaction temperatures above 548 K (Table S4, ESI†) to achieve HC formation rates comparable to the Fe site temperature (~452 K, Fig. 2C) and the observed rate of 0.24 mmol h⁻¹ g_{cat}⁻¹ (Table 1c) in this study. Under CO₂ photoreduction conditions, Fe sites remained exclusively in the Fe⁰ state (Fig. 2A and B), whereas thermal CO₂ reduction commonly involves Fe oxides and carbides (Table S4, ESI†). While the initial reduction of the first O atom in CO₂ over Fe⁰ surfaces¹⁹ typically requires high temperatures (>548 K),²⁰ this study demonstrates that the first reduction step was instead facilitated by charge separation at V_O^{••} sites on the ZrO₂ surface under light irradiation, enabling the reaction:



as previously reported.⁹ This step was particularly effective at lower light intensities (110–322 mW cm⁻²; Table 1a–b') in the presence of neighboring Fe⁰ nanoparticles. The subsequent hydrogenation pathway, where COH migrates to Fe⁰ and undergoes further reduction to C₁₋₃ HCs, is likely a common feature in both thermal (Table S4, ESI†) and photo (~452 K, Fig. 2C) reactions, regardless of whether H₂ or H₂O serves as the reductant.

The authors are grateful for the financial support from the Grant-in-Aid for Scientific Research B (24K01522, 20H02834, YI) from the Japan Society for the Promotion of Science. X-ray absorption experiments were performed with the approval of

the Photon Factory Proposal Review Committee (2024G067, 2022G527, 2021G546). The authors would like to thank Enago (www.enago.jp) for the language review.

Data availability

The supporting data have been included as part of the ESI.†

Conflicts of interest

There are no conflicts to declare.

References

- 1 Y. Izumi, *Coord. Chem. Rev.*, 2013, **257**, 171–186.
- 2 Y. Izumi, in *Advances in CO₂ Capture, Sequestration, and Conversion*, ed. F. Jin, L.-N. He and Y. H. Hu, ACS Symposium Series, ACS Publications, 2015, ch. 1, vol. 1194, pp. 1–46.
- 3 T. Loumissi, R. Ishii, K. Hara, T. Oyumi, I. Abe, C. Li, H. Zhang, R. Hirayama, K. Niki, T. Itoi and Y. Izumi, *Angew. Chem., Int. Ed.*, 2024, **63**, e202412090.
- 4 J. Albero, Y. Peng and H. Garcia, *ACS Catal.*, 2020, **10**, 5734–5749.
- 5 L. H. M. de Groot, A. Ilic, J. Schwarz and K. Wärnmark, *J. Am. Chem. Soc.*, 2023, **145**, 9369–9388.
- 6 H. Zhang, T. Itoi, T. Konishi and Y. Izumi, *Angew. Chem., Int. Ed.*, 2021, **60**, 9045–9054.
- 7 H. Zhang, T. Itoi, K. Niki, T. Konishi and Y. Izumi, *Catal. Today*, 2020, **356**, 544–556.
- 8 H. Zhang, T. Itoi, T. Konishi and Y. Izumi, *J. Am. Chem. Soc.*, 2019, **141**, 6292–6301.
- 9 K. Hara, M. Nozaki, T. Hirayama, R. Ishii, K. Niki and Y. Izumi, *J. Phys. Chem. C*, 2023, **127**, 1776–1788.
- 10 A. Bouafia, S. E. Laouini, A. Khelef, M. L. Tedjani and F. Guemari, *J. Cluster Sci.*, 2021, **32**, 1033–1041.
- 11 Provided by Dr. Y. Niwa, High Energy Accelerator Research Organization.
- 12 C. R. Kwawu, R. Tia, E. Adei, N. Y. Dzade, C. R. A. Catlow and N. H. de Leeuw, *Phys. Chem. Chem. Phys.*, 2017, **19**, 19478–19486.
- 13 S. E. Collins, M. A. Baltanas and A. L. Bonivardi, *J. Catal.*, 2004, **226**, 410–421.
- 14 B. J. Kip, F. B. M. Duivenvoorden, D. C. Koningsberger and R. Prins, *J. Catal.*, 1987, **105**, 26–38.
- 15 *American Institute of Physics Handbook*, ed. D. E. Gray, B. H. Billings, H. P. R. Frederikse, D. F. Bleil, R. B. Lindsay, R. K. Cook, J. B. Marion, H. M. Crosswhite and M. W. Zemansky, McGraw-Hill, New York, USA, 1972, 3rd edn, pp. 4–115.
- 16 D. P. Jackson, *Surf. Sci.*, 1974, **43**, 431–440.
- 17 L. Ankudinov, B. Ravel, J. J. Rehr and S. D. Conradson, *Phys. Rev. B: Condens. Matter Mater. Phys.*, 1998, **58**, 7565–7576.
- 18 M. Vaarkamp, H. Linders and D. Koningsberger, *XDAP Version 3.2.9*, XAFS Services International, Woudenberg, The Netherlands, 2022.
- 19 L. Krauser, Q. W. Yang and E. V. Kondratenko, *ChemCatChem*, 2024, **16**, e202301716.
- 20 C. R. Kwawu, A. Aniagyei, R. Tia and E. Adei, *Mater. Renew. Sustainable Energy*, 2020, **9**, 4.

